Super-Resolution Methods in MRI: Can They Improve the Trade-Off Between Resolution, Signal-to-Noise Ratio, and Acquisition Time?

Esben Plenge,[1,2]* Dirk H. J. Poot,[1,2] Monique Bernsen,[3] Gyula Kotek,[3] Gavin Houston,[3] Piotr Wielopolski,[3] Louise van der Weerd,[4,5] Wiro J. Niessen,[1,2,6] and Erik Meijering[1,2]

Improving the resolution in magnetic resonance imaging comes at the cost of either lower signal-to-noise ratio, longer acquisition time or both. This study investigates whether so-called super-resolution reconstruction methods can increase the resolution in the slice selection direction and, as such, are a viable alternative to direct high-resolution acquisition in terms of the signal-to-noise ratio and acquisition time trade-offs. The performance of six super-resolution reconstruction methods and direct high-resolution acquisitions was compared with respect to these trade-offs. The methods are based on iterative back-projection, algebraic reconstruction, and regularized least squares. The algorithms were applied to low-resolution data sets within which the images were rotated relative to each other. Quantitative experiments involved a computational phantom and a physical phantom containing structures of known dimensions. To visually validate the quantitative evaluations, qualitative experiments were performed, in which images of three different subjects (a phantom, an ex vivo rat knee, and a postmortem mouse) were acquired with different magnetic resonance imaging scanners. The results show that super-resolution reconstruction can indeed improve the resolution, signal-to-noise ratio and acquisition time trade-offs compared with direct high-resolution acquisition. Magn Reson Med 000:000–000, 2012. © 2012 Wiley Periodicals, Inc.

Key words: magnetic resonance imaging; super-resolution; reconstruction; image quality

A fundamental consideration in any MRI experiment is how to optimally balance image resolution, signal-to-noise ratio (SNR), and acquisition time. These three imaging parameters are highly interdependent: higher resolution allows one to observe smaller details, but typically reduces SNR, and/or increases imaging time. At the same time, a certain minimum level of SNR is required to distinguish the signal of interest from system noise, and scan time should be kept low, as MR imaging resources are limited, costly, and long scan times are uncomfortable for the patient, and induce motion artifacts in the images. Together, the three parameters span a space, and their theoretical relations are well known (1). Techniques such as parallel MRI (2,3), PROPELLER (4), and compressed sensing (5) affect these relations at the acquisition level. An interesting alternative is to use super-resolution reconstruction (SRR) methods that combine acquisition strategy with post-processing.

SRR is the process of producing a high-resolution (HR) image from a sequence of low-resolution (LR) images, where each LR image transforms and samples the HR scene in a distinct fashion. The idea was first introduced in the 1980s (6) and has since grown into a research field of its own (7–9). The first example of SRR applied to MRI was described in a 2001 patent (filed in 1997) (10). While SRR methods have been studied in MRI for different applications, most work has concentrated on brain MRI (11–17). This can be attributed to the fact that SRR is highly dependent on accurate registration of the LR images (18,19), and in brain MRI a simple global motion model can be applied.

Recently, an SRR scheme based on rotation (rather than translation) of the slice selection direction was extensively investigated in (20). This scheme, yielding a more effective sampling of the k-space, allowed the use of algebraic reconstruction techniques from computed tomography, and the results confirmed the superiority of rotated slice stacks for SRR. The idea of (20) was extended to slice stacks of arbitrary orientations and displacements in (21) where they used a regularized reconstruction method and an efficient affine image transform to reduce resampling artifacts.

While SRR in MRI is a developing field, showing its potential in resolution enhancement (22), a major question from the MRI community is whether SRR has any advantage over direct HR acquisition when SNR and acquisition times are taken into account. In this work, we experimentally compare the performance of various SRR methods, and investigate their ability to improve the trade-off between the mentioned imaging parameters compared to direct HR acquisition. After reviewing theoretical aspects of SRR in MRI, we briefly describe the six SRR methods used in our investigation, and present our evaluation framework. The SRR methods have been selected as being representative of the work in SRR in MRI to this day. The

evaluation of the methods is based on both phantom data (allowing quantitative comparisons) and on real image data (allowing qualitative assessment).

THEORY

Super-Resolution in MRI

There is consensus (23,24) that super-resolution in MRI is not achievable in-plane, nor in true 3D acquisitions, since the Fourier encoding scheme excludes aliasing in frequency and phase encoding directions. However, when image contrast requirements yield long repetition times (TR) (as in, e.g., T_2-weighted images), it will be significantly faster to acquire 2D slice stacks than to acquire true 3D volumes, since the acquisition of the slices can be interleaved. In 2D slice stacks, the individual slices are Fourier encoded, but in the through-plane direction there are no inherent limitations on the frequency spectrum, and aliased frequencies may potentially be recovered. The amount of aliasing depends on the slice profile which ideally is a rect function for nonoverlapping slices. However, since the slice profile is determined by the Fourier transform of the finite length slice selection pulse, it will be only an approximation of the rect function. Because of the aliasing present when the object is convolved with the slice profile, SRR is possible.

Several strategies can be adopted when acquiring data for an SRR experiment. We argue, that by acquiring the LR data with rotational increments between the images, as introduced in (20), a more effective sampling of k-space is achieved than by shifting the LR images by sub-pixel distances along the slice selection direction. The latter approach corresponds to increasing the sampling density of the object after convolving it with the slice excitation profile. The signal is thus merely oversampled. If, on the other hand, the slice selection direction is rotated between each LR image, then the narrow slice selection direction bandlimit of each image is oriented in a different direction of the 3D frequency spectrum of the imaged object. In this case, the LR data set will contain high spatial frequencies in all three dimensions.

In a typical T_2-weighted MR experiment, with an echo time (TE) of 50 ms and a TR of 2500 ms, a maximum of about 40 slices can be acquired within the TR. To reduce the slice thickness for a given volume (which is equivalent to increasing the number of slices), while keeping the contrast (TR and TE) and the in-plane resolution fixed, the only option is to partition the volume into a number of slice packages, N_{SP}, and excite them one at a time. In this way, the acquisition time increases by a factor N_{SP}. However, the slice thickness, and thus N_{SP}, is limited by SNR requirements and the performance of the gradient. The SNR in the final image can be improved by averaging a number of acquisitions, N_{avg}. When an MR experiment is constrained as described earlier, its total acquisition time T_{acq} is given by

$$T_{acq} = TR \cdot N_{PE} \cdot N_{SP} \cdot N_{avg}, \qquad [1]$$

where N_{PE} is the number of phase encoding steps. The SNR depends not only on N_{avg} but also on the slice thickness, h:

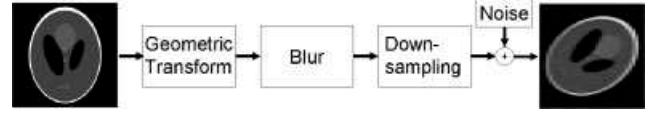$$SNR \propto h\sqrt{N_{avg}}. \qquad [2]$$

FIG. 1. The imaging model assumed in super-resolution reconstruction. Low-resolution images (right) are the result of geometric transformation, blurring, and down-sampling of high-resolution images (left), and the addition of noise.

The Imaging Model

Since SRR is an inverse problem, it requires an acquisition model to estimate the HR image underlying the LR images. The imaging model consists of three distinct submodels: a parameterization of the object space, a model of the physical acquisition process, and a statistical model that appropriately describes the noise. An MRI image can be parameterized by a vector $\mathbf{x}$ of pixels (2D) or voxels (3D). The model of the acquisition process $\mathbf{A} = \mathbf{DBM}$ decomposes into a linear operator $\mathbf{M}$, which describes a geometric transform, a linear space-invariant blurring model $\mathbf{B}$, and a linear downsampling operator $\mathbf{D}$ (Fig. 1). According to (25) the noise $\mathbf{n}$ in MRI can be assumed to be additive, white and gaussian when the SNR > 3. Thus, the acquisition of the kth LR image, $\mathbf{y}_k$, is described in vector form by

$$\mathbf{y}_k = \mathbf{A}_k \mathbf{x} + \mathbf{n}_k. \qquad [3]$$

Solving the inverse problem corresponds to recovering $\mathbf{x}$ given the $\mathbf{y}_k$ and $\mathbf{A}_k$. The problem can be formulated as an ordinary least squares (LS) problem,

$$\mathbf{x} = \arg\min_{\mathbf{x}} \sum_{k=1}^{N} ||\mathbf{y}_k - \mathbf{A}_k \mathbf{x}||^2, \qquad [4]$$

which, vertically concatenating matrices $\mathbf{A}_k$ into $\mathbf{A}$, vectors $\mathbf{y}_k$ into $\mathbf{y}$, and assuming a gaussian noise model, has the closed-form maximum-likelihood solution

$$\mathbf{x} = (\mathbf{A}^T \mathbf{A})^{-1} \mathbf{A}^T \mathbf{y}. \qquad [5]$$

Using additional prior knowledge about the solution, e.g., that it is smooth, Eqs. 4 and 5 generalize to

$$\mathbf{x} = \arg\min_{\mathbf{x}} \sum_{k=1}^{N} ||\mathbf{y}_k - \mathbf{A}_k \mathbf{x}||^2 + \lambda \, ||\mathbf{Cx}||^2 \qquad [6]$$

and

$$\mathbf{x} = (\mathbf{A}^T \mathbf{A} + \lambda \, \mathbf{C}^T \mathbf{C})^{-1} \mathbf{A}^T \mathbf{y}, \qquad [7]$$

respectively, where $\mathbf{C}$ is a regularization operator formalizing the prior knowledge, and λ is a scalar weight. Equation 7 is also known as the regularized LS solution.

A direct solution of Eqs. 5 and 7 is generally infeasible, since $\mathbf{A} \in \mathbb{R}^{n \times m}$, where n and m are the number of voxels in the reconstruction ($\mathbf{x}$) and in all the LR images ($\mathbf{y}$), respectively. Instead, iterative methods are usually applied to approximate the solution. In the following, we briefly review six such methods, including two iterative back-projection methods, two algebraic reconstruction methods, and two regularized LS solvers.

METHODS

Super-Resolution Reconstruction Methods

Iterative Back-Projection Methods

One approach to solving the inverse problem of SRR is to start from an initial guess of the HR image, then simulate N LR images via Eq. 3 and use the difference between the simulated and the acquired LR images to correct the HR estimate. The two steps are applied iteratively. Iterative back-projection (IBP) (26) is one such method. It solves the LS problem of Eq. 4 by

$$\hat{\mathbf{x}}^{(l+1)} = \hat{\mathbf{x}}^{(l)} + \sum_{k=1}^{N} \mathbf{H}_{\mathrm{BP}}(\mathbf{y}_k - \mathbf{A}_k \hat{\mathbf{x}}^{(l)}), \qquad [8]$$

where $\mathbf{H}_{\mathrm{BP}}$ is a back-projection kernel of choice, and superscript (l) indicates the iteration number. IBP solves the LS problem and thereby implicitly takes the gaussian noise model into account. It has been noted (8) that with $\mathbf{H}_{\mathrm{BP}} = \mathbf{A}^T$, IBP is equivalent to the steepest descent method. Our implementation follows (26) and includes the proposed heuristic stabilization and noise reduction schemes.

As a nonregularized LS solver, IBP is sensitive to outliers. An alternative method, termed robust super-resolution (RSR) (27), modifies IBP by exchanging its update term with a pixel-wise median of the errors:

$$\hat{\mathbf{x}}^{(l+1)} = \hat{\mathbf{x}}^{(l)} + N * \mathrm{median}\{\mathbf{H}_{\mathrm{BP}}(\mathbf{y}_k - \mathbf{A}_k \hat{\mathbf{x}}^{(l)})\}_{k=1}^{N}. \quad [9]$$

RSR approximates IBP and thus the LS solution. However, no analytical solution exists for this method.

Algebraic Reconstruction Methods

The classic algebraic reconstruction technique (ART) is a special case of the projection onto convex sets (POCS) methods (28,29). It was introduced in image processing by Gordon et al. (30). ART starts from an initial guess, $\hat{\mathbf{x}}^{(0)}$, and then iteratively updates $\hat{\mathbf{x}}$ one pixel at a time, via

$$\hat{\mathbf{x}}_j^{(l+1)} = \hat{\mathbf{x}}_j^{(l)} + \lambda^{(l)} \frac{\mathbf{y}_i - \langle \mathbf{a}_i, \hat{\mathbf{x}}^{(l)} \rangle}{\|\mathbf{a}_i\|_2^2} \mathbf{a}_{ij}, \qquad [10]$$

where $\hat{\mathbf{x}}_j^{(l)}$ denotes the jth element in $\hat{\mathbf{x}}$ in the lth iteration, $\mathbf{a}_i$ is the ith row of $\mathbf{A}$, and $\mathbf{a}_{ij}$ is the (i, j)th element of $\mathbf{A}$. ART converges to the minimum norm solution (31), satisfying

$$\hat{\mathbf{x}} = \arg\min_{\mathbf{x}} \|\mathbf{x}\|_2^2 \quad \text{subject to} \quad \mathbf{A}\mathbf{x} = \mathbf{y}, \qquad [11]$$

the minimum L_2 norm thus functioning as a regularizer.

An ART implementation is easily extended into POCS by applying constraints to Eq. 10 at each projection step l. In our implementation, we applied amplitude and energy constraints as described in (29).

Regularized Least Squares Methods

The term $\mathbf{C}$ in Eq. 6 should incorporate prior knowledge about the solution. When it does, the method is known as Tikhonov regularization. The regularization term is usually some norm of an operation (e.g., identity, first and second order derivative, Laplacian) on the HR estimate $\hat{\mathbf{x}}$. Regularization makes the underdetermined problem of SRR less ill-posed, but has the undesirable effect of smoothing sharp features in the image, such as step edges. In our implementation of a Tikhonov-regularized LS solver (TIK), we used the L_2-norm of the second order derivative of the HR reconstruction as our regularization term:

$$\|\mathbf{C}\mathbf{x}\|^2 = \left(\frac{\partial^2 \mathbf{x}}{\partial r_1^2}\right)^2 + \left(\frac{\partial^2 \mathbf{x}}{\partial r_2^2}\right)^2 + \left(\frac{\partial^2 \mathbf{x}}{\partial r_3^2}\right)^2, \qquad [12]$$

where r_i is the spatial dimension over which the partial derivative is taken. We used an average of the aligned and upscaled LR images as the initial HR estimate. The regularized LS problem of Eq. 6 was solved with the conjugate gradient method and the transforms in $\mathbf{A}$ and $\mathbf{A}^T$ were implemented using bilinear interpolation.

A recently proposed alternative SRR method (LASR) (21) also uses Eq. 12 for regularization and the conjugate gradient method for solution of Eq. [6]. However, this method applies $\mathbf{A}$ and $\mathbf{A}^T$ by an affine transformation scheme that minimizes aliasing and spectral distortions.

The experiments with TIK and LASR in this study, were all performed with little regularization ($\lambda = 0.004$), except for the in vivo experiments where $\lambda = 0.01$. These values were found by experimenting with a range of λ-values and qualitatively determining the best result.

Evaluation Framework

To evaluate whether SRR methods can decrease the slice thickness of MR images at better SNR and timing trade-offs than direct HR acquisition, we devised an evaluation framework, using the relations established earlier (Eqs. 1 and 2): (1) for fixed field-of-view (FOV) and N_{avg}, the acquisition time scales inversely with slice thickness, (2) for a fixed N_{avg} the SNR scales linearly with slice thickness, and (3) for a given slice thickness, h, the SNR increases with N_{avg} and thus, using Eq. 1, with the acquisition time by $\sqrt{T_{\mathrm{acq}}}$.

Quantitative Experiments

To quantitatively evaluate the performance of the SRR methods, two types of data were used: (1) simulated acquisitions based on the well-known computer generated Shepp-Logan phantom (SLP) and (2) MRI images of a Varian phantom.

Simulations. The SLP experiments were performed to investigate the situation in which the acquisition model is known exactly. In total, 24 anisotropic reformatted LR slices of 128×32 pixels (frequency encoding direction $\times$ slice selection direction) were simulated from a 512×512 pixel image, using rotation around the image center (and the virtual phase encoding axis) in increments of 180/24 degrees (see Fig. 2). Gaussian noise was added, such that the SNR was around 32 dB, which is within the realistic range for an MRI experiment. From the 24 LR images, eight subsets were created containing $n = 1, 2, 3, 4, 6, 8, 12$, and 24 images, respectively, such that the rotation increments within the subsets were 180/n degrees. From each of these subsets, images of 128×128 pixels were produced
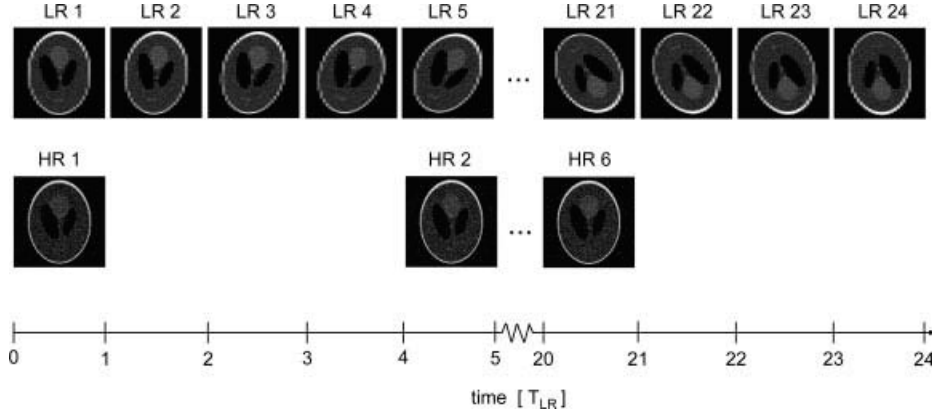
FIG. 2. Illustration of the simulation and acquisition scheme of the quantitative experiments. Upper row: 24 LR images are simulated/acquired while rotating the FOV around the phase-encoding axis in increments of 24/180 degrees. Lower row: Six HR images of four times thinner slices and four times longer acquisition time than the LR images are simulated/acquired, enabling postacquisition production of multiple averages images. Note that the image planes shown (both LR and HR) are spanned by the frequency encoding and slice selection directions. The unit of the time axis is T_{LR}, the acquisition time of a single LR image.

by each of the six SRR algorithms, and by using a bilinear interpolation scheme (INT). To simulate direct HR acquisition (DAC), six images of 128×128 pixels, covering the same 2D FOV as the LR simulations, were also produced from the 512×512 pixel image, again by applying the imaging model. Averaging these images improves the SNR of the resulting image. According to the inverse relation between slice thickness and acquisition time, six averaged HR images take the same acquisition time as 24 LR images with four times thicker slices, see Fig. 2. This allowed us to compare the SRR images with the averaged HR images within the same "acquisition time" range.

MRI phantom acquisitions. A corresponding MRI experiment was performed using the phantom, containing liquid-filled structures (water doped with copper sulfhate) yielding homogeneous signal, surrounded by plastic and air, resulting in signal void. LR data were acquired using a T_2-weighted 2D fast spin echo (FSE) sequence on a clinical GE 3T system. TR was 2100 ms, TE was 27.4 ms, with an $N_{avg} = 1$ and $N_{SP} = 1$. The slice stack consisted of 18 slices (4 mm thick) with a FOV of 128×128 mm, $N_{PE} = 128$, and a resolution of $1.0 \times 1.0 \times 4.0$ mm. The scan time per stack (T_{LR}) was 73 s. The experiment was repeated 24 times, while the slice stack was rotated around the phase encoding direction in increments of approximately 180/24 degrees.

For analysis, eight subsets were picked from the 24 slice stacks containing $n = 1, 2, 3, 4, 6, 8, 12$, and 24 stacks, respectively. Each subset was selected such that the rotational increments between its slice stacks were approximately equal. If we denote the acquisition time of one LR image by T_{LR}, each subset thus had an acquisition time of $n\,T_{LR}$. Reconstruction of 1 mm isotropic resolution images from the eight LR subsets allowed evaluating resolution and SNR as a function of the acquisition time in the reconstructed images.

For quantitative comparison, isotropic reference images were acquired directly at 1 mm slice thickness. Having four times thinner slices than the LR images but the remaining imaging parameters identical to those of the LR images, these required an acquisition time of $4\,T_{LR}$ each. For a given

imaging sequence and resolution, conventional MRI can improve the SNR only by averaging multiple images. Imaging time increases linearly with the number of averaged images (Eq. 1). This way, the quality of direct acquisitions (DAC) could be evaluated at time points that were multiples of $4\,T_{LR}$ and spanned the same time range as the reconstructed images, Fig. 2.

Quantitative evaluation measures. We assessed the performance of the six described SRR methods: IBP, RSR, ART, POCS, TIK, and LASR. We compared the SRR methods to simple bilinear interpolation of the data sets (INT) and to directly acquired HR data sets (DAC). Resolution (in millimeters) was measured in each image as the average width of 20 edge profiles, see Fig. 3. The edge width of each profile was computed by nonlinear LS fitting of the following sigmoid function (12,20):
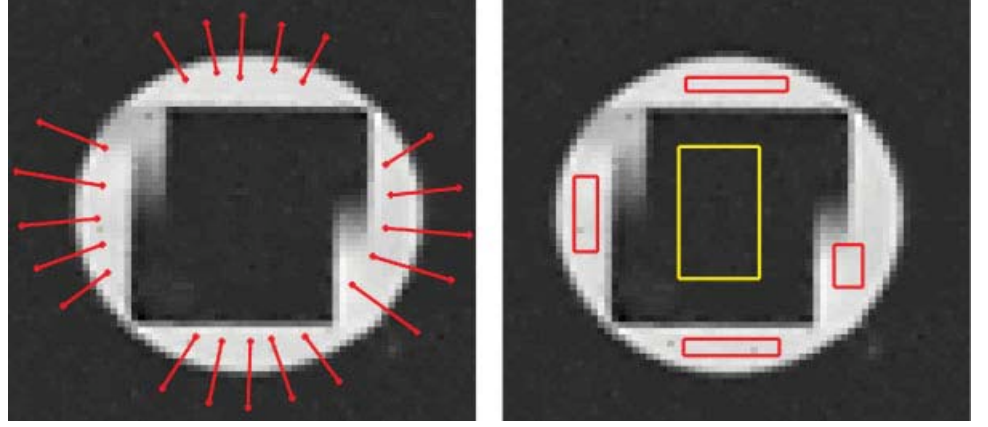
$$f = a_1 + \frac{a_2}{1 + \exp(-a_3(x - a_4))}, \qquad [13]$$

where $4.4/a_3$ is the width of the curve's rise length from 0.1 to 0.9 for normalized intensity values ($a_3 = 4.4$ corresponds to a rise length of 1 pixel). The SNR of the evaluation images was computed by dividing the mean of four high-intensity foreground regions with the standard deviation of a background region. The foreground and background regions-of-interest used for the calculation are visualized in Fig. 3.

Qualitative Experiments

To qualitatively evaluate the capabilities of the SRR methods, four LR data sets were acquired of four different samples, using three different scanners. In all cases, the LR images were acquired just above the scanner systems' lower limits on slice thickness. Reconstructions of HR images were thus aiming at surpassing these limits. As references, to assess the quality of the reconstructions, data sets were acquired, where the plane of interest in the reconstructions were captured in-plane.

FIG. 3. The edge width measures are based on the intensity profile of 20 edge-crossing strips as illustrated in the left figure. The SNR calculations are based on the high-intensity regions and one background region as illustrated in the right figure.

Phantom. The same phantom as described earlier was scanned using a T_2-weighted 2D fast spin echo (FSE) sequence on a clinical GE 3T system. TR was 2100 ms, TE was 36.5 ms, with $N_{avg} = 1$ and $N_{SP} = 1$. The 2D slice stack consisted of 36 slices (2 mm thick), with a FOV of 128×128 mm, $N_{PE} = 256$, and a resolution of $0.5 \times 0.5 \times 2.0$ mm. The scan time per stack was 278 s. The experiment was repeated 12 times, while the slice stack was rotated around the phase encoding axis in increments of ~180/12 degrees. SRR was performed on an isotropic HR grid of resolution $0.5 \times 0.5 \times 0.5$ mm.

Postmortem mouse. A whole-body scan of a postmortem mouse was acquired on a 7T Bruker Pharmascan system using a recovery FSE (frFSE) sequence. TR was 6648 ms, TE was 33 ms, with $N_{avg} = 1$ and $N_{SP} = 1$. The 2D slice stack consisted of 64 slices (0.5 mm thick), with a FOV of 50×32 mm, and a resolution of $0.125 \times 0.125 \times 0.5$ mm. The scan time per stack was 213 s. The slice stack was rotated around the phase encoding axis in 24 uniform increments of 180/24 degrees. Because of the scanner's limited FOV, the mouse was scanned in three sections (head, chest, and lower abdomen). SRR was performed on each section separately on isotropic HR grids of resolution $0.125 \times 0.125 \times 0.125$ mm.

Ex vivo rat knee. An ex vivo rat knee, into which cells labeled with super-paramagnetic iron oxide (SPIO) particles were injected, was acquired on a 7T Varian animal system with a fast recovery FSE (frFSE) sequence. TR was 5600 ms, TE was 7.1 ms, with $N_{avg} = 1$ and $N_{SP} = 1$. The 2D slice stack consisted of 24 slices (0.4 mm thick), with a FOV of 26×26 mm, $N_{PE} = 256$ and a resolution of ~$0.1 \times 0.1 \times 0.4$ mm. The scan time per stack was 252 s. The slice stack was rotated around the phase encoding axis in 12 increments of ~180/12 degrees. SRR was performed on an isotropic HR grid of resolution $0.1 \times 0.1 \times 0.1$ mm.

In vivo mouse brain. To gain preliminary insight into the potential of in vivo application of SRR in MRI, brain images of a living mouse were acquired on a 7T Bruker Pharmascan system using a RARE T_1 weighted spin echo sequence. TR was 680 ms, TE was 8.7 ms, $N_{avg} = 4$, and $N_{SP} = 1$. The 2D slice stack consisted of 21 slices (0.5 mm thick), with a FOV of 150×256 mm, $N_{PE} = 150$ and a resolution of ~$0.1 \times 0.1 \times 0.5$ mm. The scan time per stack was 210 s. The slice stack was rotated in eight increments of ~180/8 degrees around the frequency encoding axis.

SRR was performed to an isotropic HR grid of resolution $0.1 \times 0.1 \times 0.1$ mm. As a reference for the anatomical structures seen in the reconstructions, a RARE 3D T_1 weighted gradient echo image was included in the experiment. The resolution was $0.1 \times 0.1 \times 0.1$ mm, TR was 30 ms, TE was 3.6 ms, and $N_{avg} = 4$.

RESULTS

Quantitative Results on Simulations

The evaluation results of the simulation experiment are summarized in Fig. 4, which shows the resolution and SNR of the SLP reconstructions versus "acquisition time." All SRR methods achieve large resolution improvements for acquisition times up to 4 T_{LR}. Especially the regularized least-squares methods (TIK, LASR), and the iterative back-projection methods (IBP, RSR) achieve substantial resolution improvements, around a factor 2; the algebraic reconstruction methods (ART, POCS) in contrast, result in far less resolution gain. Beyond 4 T_{LR} LASR, IBP, and RSR reconstructions show only modest resolution gains. Only the TIK reconstructions eventually achieve a resolution of 1 mm. This happens around 10 T_{LR}, and at 24 T_{LR} the resolution is around 0.83 mm. The measured resolution of the directly simulated HR images (DAC) is around 1.18 mm for all time points. It is surpassed by TIK reconstructions around 6 T_{LR}. Standard bilinear interpolation (INT) has virtually no resolution enhancing capabilities. In terms of SNR, both IBP and RSR reconstructions show considerable improvement over the entire time range. TIK, LASR, and ART reconstructions show a modest upward trend, while the SNR improvement of the POCS reconstructions is more pronounced. INT images have a high SNR that increases with increased acquisition time.

Quantitative Results on Phantom MRIs

The performance of the six SRR methods, bilinear interpolation, and direct acquisition on the Varian phantom data is shown in Fig. 5. The general trends are similar to those found with the SLP reconstructions. Only the SNR curves of TIK and LASR reconstructions are different between the SLP and Varian plots. For reference, the graphs also include the theoretical curves (THEO) of isotropic 1.2, 1.3, and 1.4 mm resolution images. It can be observed that the
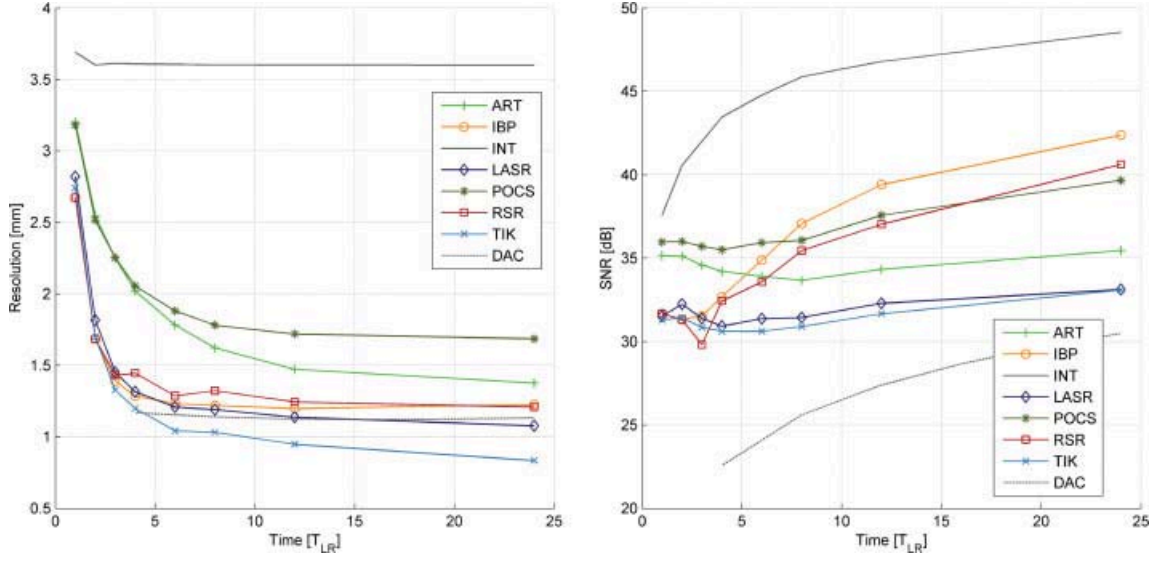
FIG. 4. Resolution (left) and SNR (right) of the six SRR methods and bilinear interpolation (solid curves) as a function of acquisition time compared to direct HR imaging (dashed curves) for the computer generated SLP data. The unit of time along the x-axis is T_{LR} (the time required to acquire one LR image).

TIK reconstructions surpass the measured resolution of the DAC images around 15 T_{LR} while its SNR at that point is more than 6 dB higher than that of the DAC images. Furthermore, it can be observed how TIK reconstructions reach a resolution of 1.2 mm already at 5 T_{LR}. For acquisition times beyond 12 T_{LR}, the measured resolution of IBP reconstructions is around 1.2 mm, while the SNR for this method at 12 T_{LR} is 3.0 dB higher than that of a direct acquisition of 1.2 mm isotropic resolution. At 24 T_{LR}, this difference is even 4.8 dB. From 4 T_{LR} to 8 T_{LR}, the IBP reconstructions reach a measured resolution of approximately 1.3 mm, while the corresponding SNRs are only slightly (0.5-0.8 dB) higher than that of the theoretical 1.3 mm resolution image.

Qualitative Results

The results of the three qualitative experiments are presented in Figs. 6–8. The images in Fig. 6 show a detail of radial lines from the Varian phantom and confirm the quantitative results presented in the previous section. The striking improvement in resolution achievable by SRR is clear by comparison with the reference anisotropic LR image, in which the lines can be resolved only when they are perpendicular to the HR dimension of the image. Moving along the radial lines toward the center, at some point the ability to resolve the lines is lost. This point occurs earlier for the reconstructions than for the image where the
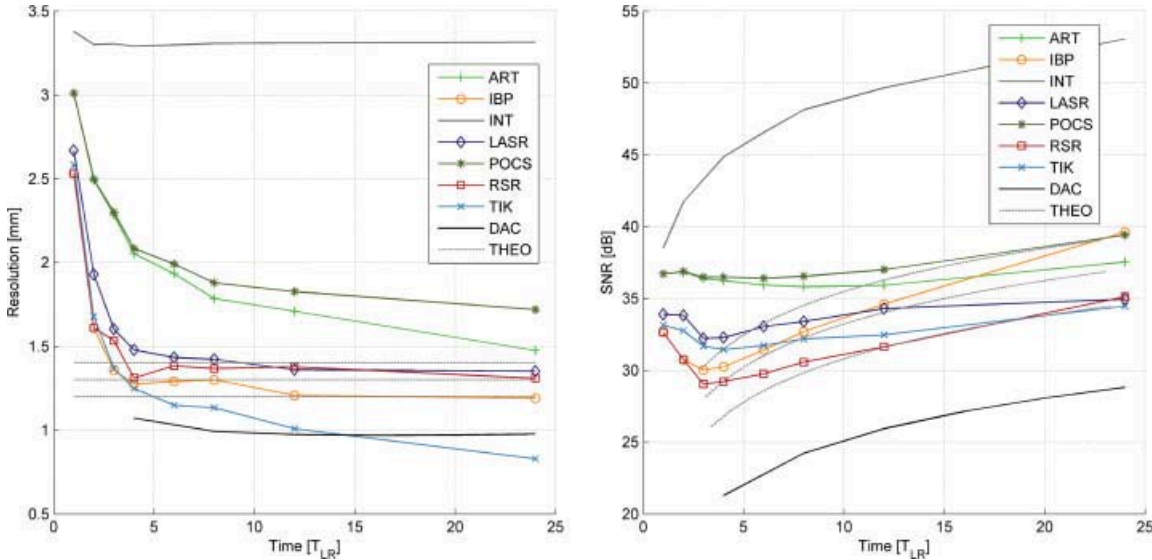

FIG. 5. Resolution (left) and SNR (right) of the six SRR methods and bilinear interpolation (solid curves) as a function of acquisition time compared to direct HR imaging at 1 mm (black curve) and 1.2, 1.3, 1.4 mm (from lower to upper dashed curves) for the MRI data of the physical Varian phantom. The unit of time along the horizontal axis is T_{LR} (the time required to acquire one LR image).
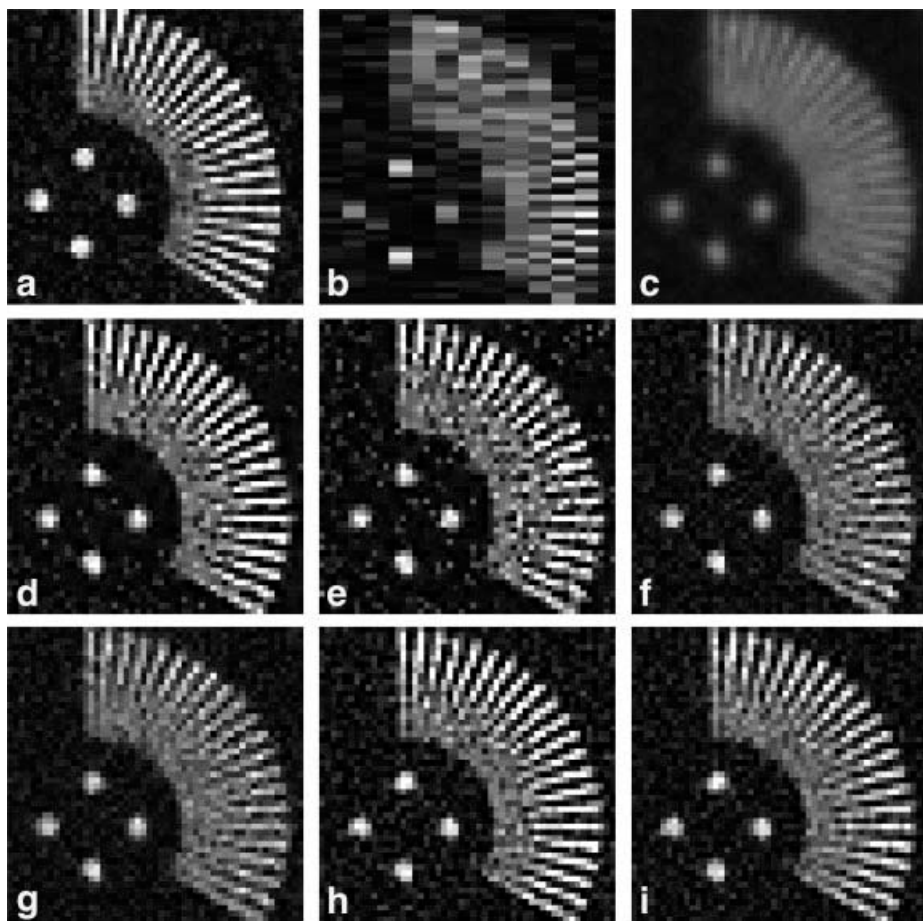
FIG. 6. Visual impression of the performance of the SRR methods on the Varian phantom data. The panels show: (**a**) the structure of interest in the HR plane of a direct acquisition, (**b**) the structure of interest in the LR plane, and the results of (**c**) INT, (**d**) IBP, (**e**) RSR, (**f**) ART, (**g**) POCS, (**h**) TIK, and (**i**) LASR, based on 12 LR images. The intensities of each image have been scaled according to the mean value of a homogeneous high-intensity region in the image.
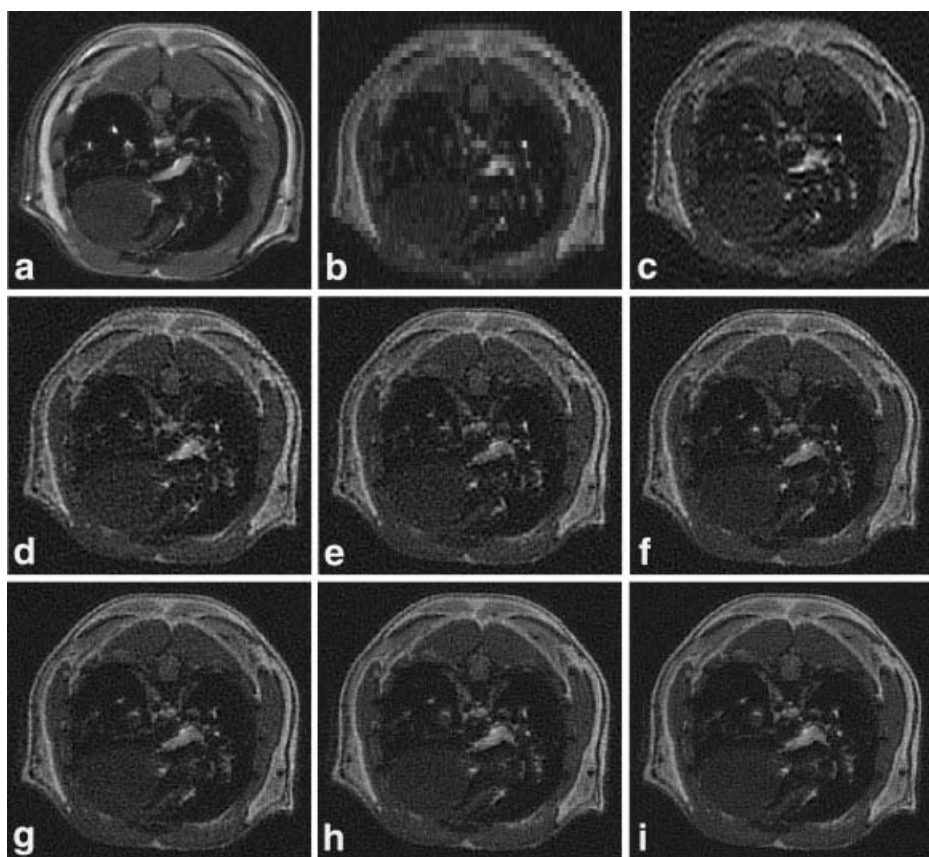
FIG. 7. Axial slices of the full-body mouse scan. The images show: (**a**) a slice from a direct acquisition with thick slices but high resolution in the plane shown, (**b**) one of the LR acquisitions, and the results of TIK using (**c**) 2, (**d**) 3, (**e**) 4, (**f**) 6, (**g**) 8, (**h**) 12, and (**i**) 24 LR images.
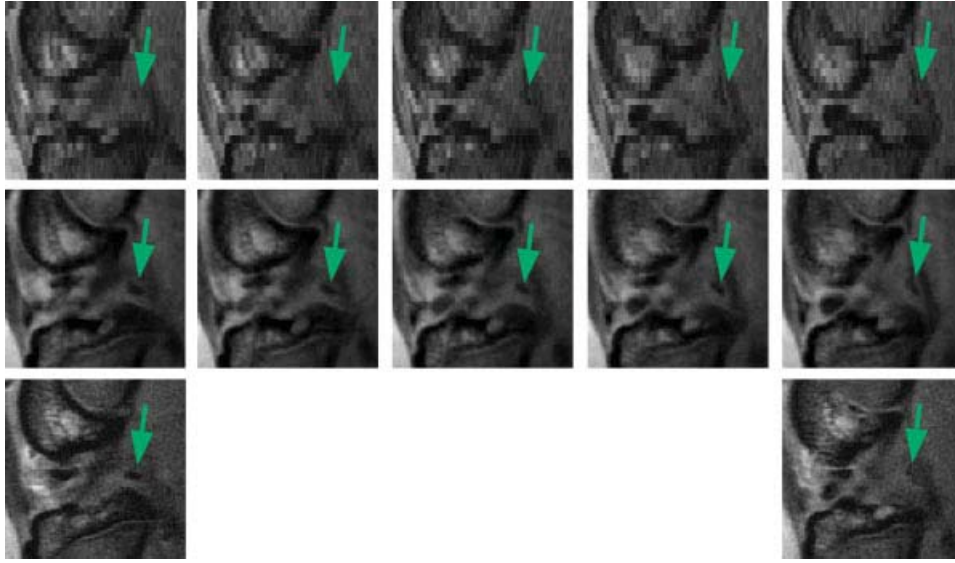
FIG. 8. Potential of SRR demonstrated on ex vivo data of a rat knee with SPIO-labeled cells (green arrows). Top row: a sequence of reformatted 2D slices of anisotropic LR acquisition. Middle row: corresponding SRR slices, reconstructed using 12 LR images and the TIK method. Bottom row: two slices of anisotropic reference acquisition with target resolution in the plane reconstructed above. The three sequences all cover approximately the same spatial volume.

radial lines are captured in-plane, showing that the latter still has somewhat higher resolution in that plane. The TIK and IBP reconstructions, which had the highest resolution in the quantitative evaluation, are sharper than the other reconstructions, and have good contrast. Over the entire time range, we found that TIK and LASR reconstructions were the most qualitatively pleasing.

Figure 7 shows the results of the experiments (reconstructed with TIK) on a postmortem mouse. The sample axial slices demonstrate that the quality of the reconstructions clearly improves when an increasing number of LR images is used. In agreement with the results of the quantitative experiments, it can be observed that the quality improvement is substantial going from 2 to 8 LR images, while a smaller effect is seen when going from 12 to 24 LR images. Again, the highest resolution is achieved by direct acquisition with the slice of interest in-plane.

Sample results (reconstructed with TIK) of the experiments on an ex vivo rat knee with SPIO-labeled stem cells inside are shown in Fig. 8. The cell cluster is visible as
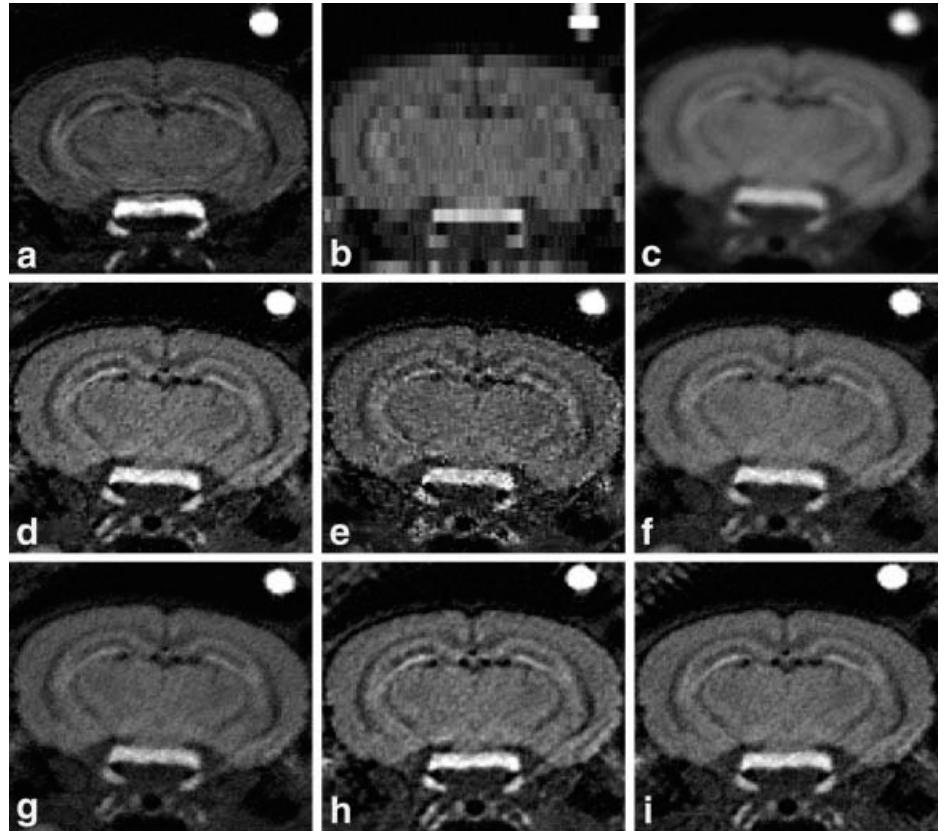

FIG. 9. Axial slices of in vivo mouse brain. The images show: (**a**) a direct HR 3D acquisition, (**b**) one of the eight LR acquisitions, and reconstructions with (**c**) INT, (**d**) IBP, (**e**) RSR, (**f**) ART, (**g**) POCS, (**h**) TIK, and (**i**) LASR, using eight LR images.

a darker shadow in the sequence of reformatted LR slices (top row). In the sequence of SRR images (middle row) the cell cluster is considerably better visualized. The bottom row shows an LR acquisition where the slice selection and phase encoding directions were interchanged such that the FOV of the reformatted images in the top row was captured in-plane. In the first of these two slices, the cell cluster is clearly visible. However, the distance between consecutive slices is large, and in the second slice the cell cluster is hardly visible.

Finally, the results of the in vivo mouse brain experiments are shown in Fig. 9. The reconstructions of all tested methods are included and show characteristics similar to those of the MRI phantom. In all cases, a clear improvement is seen from the LR images to the reconstruction results. TIK and LASR reconstructions are sharper than ART and POCS reconstructions, and less noisy than IBP and RSR reconstructions. The LASR reconstruction is slightly smoother than that of TIK. Comparing with the isotropic 3D acquisition, the reconstructions reproduce the anatomical structures seen in that image with a reasonable degree of accuracy.

DISCUSSION

In this study, we have shown that SRR indeed provides advantages over direct HR acquisition when SNR and acquisition time are taken into account. While the performance of SRR compared with that of direct acquisitions has been studied before (12), no framework has previously been presented in the literature that allows thorough analysis of the relations between resolution, SNR, and acquisition time. So far, the net practical advantage of using SRR has thus remained unclear. To enable a thorough investigation of this, we designed the evaluation framework presented in this work. Image quality evaluation is notoriously tricky, the quality cannot be captured by any one single measure. In our framework, we therefore included both quantitative and qualitative comparisons between SRR and direct HR acquisitions.

Our quantitative results suggest that SRR enables surpassing the resolution achieved by direct HR acquisition. This confirms the results of (12). Quantitative experiments (Fig. 5) show that the reconstructions of one SRR method (TIK) surpasses the resolution of the direct HR acquisition, while having substantially higher SNR (> 6 dB) at that time point. However, comparing Fig. 6h with 6a, this result is not confirmed. The reason for this discrepancy is most likely that the TIK algorithm implicitly applies a sharpening filter and amplifies high-frequency content excessively. This results in overshoot (Gibbs ringing) artifacts at step edges in the reconstructions, causing the sigmoid function to fit to a more steeply rising edge and thus underestimate the edge width.

The IBP reconstructions do not surpass the resolution of the direction but approaches and slightly surpasses a resolution of 1.2 mm, while achieving an SNR of 3.0–4.8 dB higher than a theoretical 1.2 mm resolution direct acquisition, in the same total acquisition time. As such, the quantitative results in Figs. 4 and 5 show a clear improvement in the resolution-SNR-acquisition time trade-off.

The experimental results (in particular those illustrated in Figs. 6 and 8) highlight the benefits of isotropic resolution. When small structures are to be visualized with MRI, SRR methods can be employed to surpass the limits on slice thickness imposed by the scanner system or protocol. The LR images of all four qualitative experiments have been acquired just above the slice thickness limit and by SRR reconstructed to isotropic resolution below that limit. In this way, the use of SRR alleviates the need for careful orientation of the object or acquisition planes, relaxing experimental conditions.

The ability to compare the performance of SRR methods within the resolution-SNR-acquisition time trade-off space is an additional result of our study. In this work, we have compared six SRR methods representative of those found in the literature. The IBP and RSR methods use the data as the only constraint on the solution, while TIK and LASR incorporate prior knowledge as regularization terms. In the latter case, a smoother, lower resolution, solution can be expected. However, using low λ-values, the effect of the regularization is limited. ART and POCS yielded the overall poorest resolution results. For all six methods, we found that using as few as four LR images for the reconstruction yielded substantial improvements in resolution. This may be related to the anisotropy factor of the LR images, which was also four in our experiments.

The choice of using the phase encoding axis as the axis of rotation of the LR acquisitions was deliberate for the ex vivo mouse scans. These were acquired in three parts with a FOV smaller than the whole length of the mouse body. By choosing the orientation of the read-gradient in the head-foot direction, aliasing was avoided. This choice causes chemical shift artifacts to change between the LR images and potentially leads to blurring of the reconstructions. We have, however, not observed this effect in our experiments. By instead choosing the frequency encoding axis as the axis of rotation, the phase encoding axis changes direction in each rotated slice stack. The related change in direction of the motion blurring artifacts between the slice stacks, is expected to increase motion blurring when the subject is moving. We tested this setup in our in vivo reconstructions but did not observe pronounced blurring.

Good agreement was found between the results of the quantitative experiments on the computer generated phantom (SLP) and the real phantom (Varian) (cf. Figs. 4 and 5). The results of the qualitative experiments also confirmed the findings of the quantitative experiments (cf. Figs. 5 and 6). This is in line with a previous observation that the performance of SRR methods on real MRI data can be predicted accurately by measuring the performance on simulated data if an appropriate model of the imaging system is available (32), and suggests that for future SRR algorithm development and testing it is valid to use simulated phantoms in the initial stages and postpone costly MRI experiments to the final stages.

In vivo mouse brain experiments were included in this study to get an idea of the potential of applying SRR in more practical research settings. We deliberately did not include these experiments in the trade-off investigation, since an entirely new set of problems related to motion and blood flow are expected when working with in vivo data. The results, however, were encouraging: we did not observe

any motion related artifacts in the reconstructions, and the reconstructions reproduced the anatomical structures seen in the reference 3D acquisition with reasonable accuracy. The experiment shows that in principle SRR is possible in live animals. The brain, in particular, seems to lend itself nicely to SRR as pulsatile and breath induced motion is limited compared with in the body, and effective means for animal fixation are available. Our results opens the field for further experiments in this category.

A complete study of the performance of SRR in MRI is an immense task. Extensive quantitative and qualitative experiments have already been performed in (20), that focused on optimizing the acquisition of the LR data, considering the number of slice stacks, the slice thickness, SNR in the LR images and more. In this study, we have constrained ourselves to studying the resolution-SNR-acquisition time relationship, and kept all other parameters fixed. These constraints clearly remove much of the flexibility normally available in an MRI experiment but they are necessary to consistently investigate isolated aspects of the imaging process. Future studies of SRR in MRI should include rigorous comparisons of SRR versus specific experimental acquisition schemes (high-resolution 3D and interlaced slice acquisition schemes, different sequence etc). SRR may prove particularly useful for MRI methods that inherently suffer from long acquisition times, such as fast spin echo techniques (FSE, RARE), and inversion recovery methods (FLAIR, IR-SE), especially when SNR requirements forces the averaging of multiple acquisitions and thereby prolong the acquisition time. Apart from comparing SNR, CNR, resolution and acquisition time, future studies should also look into the experimental factors influencing the real and reconstructed image quality, such as physiological noise, pulsatile motion (heart, blood flow), slice-to-slice interference, etc.

In conclusion, we have shown that SRR is capable of providing better trade-offs between resolution, SNR and acquisition time than direct HR acquisition, and is particularly useful when limits on slice thickness and the number of slices are imposed by the scanner system or protocol. We have not been able to reproduce earlier results in which SRR reconstructions surpass the resolution of directly acquired high-resolution images, and suspect that these results could be influenced by a bias toward overshoot in the resolution measure. We have demonstrated SRRs potential in application to in vivo MRI, and provided directions for future research in SRR in MRI. Finally, by the presented evaluation framework we provide a protocol for quantitatively evaluating and comparing the performance of SRR algorithms in MRI.

REFERENCES

1. Haacke EM, Brown RW, Thomson MR, Venkatesan R. Magnetic resonance imaging. Physical principles and sequence design. New York: Wiley; 1999.
2. Heidemann RM, Özsarlak O, Parizel PM, Michiels J, Kiefer B, Jellus V, Müller M, Breuer F, Blaimer M, Griswold MA, Jakob PM. A brief review of parallel magnetic resonance imaging. Eur Radiol 2003;13:2323–2337.
3. Pruessmann K. Encoding and reconstruction in parallel MRI. NMR Biomed 2006;19:288–299.
4. Pipe JG. Motion correction with PROPELLER MRI: Application to head motion and free-breathing cardiac imaging. Magn Reson Med 1999;42:963–969.
5. Lustig M, Donoho D, Pauly JM. Sparse MRI: the application of compressed sensing for rapid MR imaging. Magn Reson Med 2007;58:1182–1195.
6. Tsai RY, Huang TS. Multi-frame image restoration and registration. In: Advances in computer vision and image processing, Vol. 1. Greenwich, CT, USA: JAI Press; 1984. pp 317–339.
7. Borman S, Stevenson RL. Spatial resolution enhancement of low-resolution image sequences: a comprehensive review with directions for future research. Technical report, Department of Electrical Engineering, University of Notre Dame, Notre Dame, Indiana, USA, 1998.
8. Elad M, Feuer A. Restoration of a single superresolution image from several blurred, noisy, and undersampled measured images. IEEE Trans Image Process 1997;6:1646–1658.
9. Park S, Park M, Kang M. Super-resolution image reconstruction: a technical overview. IEEE Signal Process Mag 2003;20:21–36.
10. Fiat D. Method of enhancing an MRI signal. U S Patent 6,294,914 (2001).
11. Peled S, Yeshurun Y. Superresolution in MRI: application to human white matter fiber tract visualization by diffusion tensor imaging. Magn Reson Med 2001;45:29–35.
12. Greenspan H, Oz G, Kiryati N, Peled S. MRI inter-slice reconstruction using super-resolution. Magn Reson Imaging 2002;20:437–446.
13. Peeters RR, Kornprobst P, Nikolova M, Sunaert S, Vieville T, Malandain G, Deriche R, Faugeras O, Ng M, Hecke PV. The use of superresolution techniques to reduce slice thickness in functional MRI. Int J Imag Syst Tech 2004;14:131–138.
14. Zhang X, Lam EY, Wu EX, Wong KK. Application of Tikhonov regularization to super-resolution reconstruction of brain MRI images. In: Medical Imaging and Informatics. Berlin, Heidelberg: Springer-Verlag; 2008. pp 51–56.
15. Rousseau F, Glenn OA, Iordanova B, Rodriguez-Carranza C, Vigneron DB, Barkovich JA, Studholme C. Registration-based approach for reconstruction of high-resolution in utero fetal MR brain images. Acad Radiol 2006;13:1072–1081.
16. Rousseau F, Kim K, C S, Koob M, Dietemann JL. On super-resolution for fetal brain MRI. In: Proceedings of the 13th International Conference on Medical Image Computing and Computer-Assisted Intervention: Part II. Berlin, Heidelberg: Springer-Verlag; 2010, p. 355–362.
17. Gholipour A, Estroff J, Warfield S. Robust super-resolution volume reconstruction from slice acquisitions: Application to fetal brain MRI. IEEE Trans Med Imaging 2010;29:1739–1758.
18. Robinson D, Milanfar P. Statistical performance analysis of super-resolution. IEEE Trans Image Process 2006;15:1413–1428.
19. Lin Z, Shum HY. Fundamental limits of reconstruction-based super-resolution algorithms under local translation. IEEE Trans Pattern Anal Mach Intell 2004;26:83–97.
20. Shilling RZ, Robbie TQ, Bailloeul T, Mewes K, Mersereau RM, Brummer ME. A super-resolution framework for 3-D high-resolution and high-contrast imaging using 2-D multislice MRI. IEEE Trans Med Imaging 2009;28:633–644.
21. Poot DHJ, Van Meir V, Sijbers J. General and Efficient Super-Resolution Method for Multi-Slice MRI. In: Proceedings of the 13th International Conference on Medical Image Computing and Computer-Assisted Intervention: Part I. Berlin, Heidelberg: Springer-Verlag; 2010. pp 615–622.
22. Greenspan H. Super-resolution in medical imaging. Comput J 2009;52:43–63.
23. Scheffler K. Superresolution in MRI? Magn Reson Med 2002;48:408.
24. Peled S, Yeshurun Y. Superresolution in MRI — Perhaps sometimes. Magn Reson Med 2002;48:409–409.
25. Gudbjartsson H, Patz S. The Rician distribution of noisy MRI data. Magn Reson Med 1995;34:910–914.

26. Irani M, Peleg S. Improving resolution by image registration. CVGIP: Graph Models Image Process 1991;53:231–239.

27. Zomet A, Rav-Acha A, Peleg S. Robust Super-Resolution. In: Proceedings of IEEE Computer Society Conference on Computer Vision and Pattern Recognition (CVPR), 2001, Kauai, HI. pp 645–650.

28. Kaczmarz S. Angenäherte Auflösung von Systemen linearer Gleichungen. Bull Acad Pol Sci Lett A 1937;355–357.

29. Stark H, Oskoui P. High-resolution image recovery from image-plane arrays, using convex projections. J Opt Soc Am A 1989;6:1715–1726.

30. Gordon R, Bender R, Herman GT. Algebraic reconstruction techniques (ART) for three-dimensional electron microscopy and X-ray photography. J Theor Biol 1970;29:471–481.

31. Herman GT, Lent A, Rowland SW. ART: Mathematics and applications. A report on the mathematical foundations and on the applicability to real data of the algebraic reconstruction techniques. J Theor Biol 1973;42:1–32.

32. van Eekeren AWM, Schutte K, Oudegeest OR, van Vliet LJ. Performance evaluation of super-resolution reconstruction methods on real-world data. EURASIP J Adv Signal Process 2007;2007:1–12.